

Article

Application of Synthesized Vanadium–Titanium Oxide Nanocomposite to Eliminate Rhodamine-B Dye from Aqueous Medium

Mohamed R. Elamin ^{1,*}, Babiker Y. Abdulkhair ^{1,2} , Nuha Y. Elamin ^{1,2}, Khalid H. Ibnaouf ³ , Hajo Idriss ³ , Rafia Bakheit ⁴ and Abueliz Modwi ^{5,*} 

¹ Chemistry Department, College of Science, Imam Mohammad Ibn Saud Islamic University (IMSIU), Riyadh 13318, Saudi Arabia

² Chemistry Department, Faculty of Science, Sudan University of Science and Technology (SUST), Khartoum P.O. Box 407, Sudan

³ Physics Department, College of Science, Imam Mohammad Ibn Saud Islamic University (IMSIU), Riyadh 13318, Saudi Arabia

⁴ Department of Physics, College of Sciences and Arts, Qassim University, Unaizah 51911, Saudi Arabia

⁵ Department of Chemistry, College of Science and Arts, Qassim University, Ar Rass 52571, Saudi Arabia

* Correspondence: mrabuzaid@imamu.edu.sa (M.R.E.); abuelizkh81@gmail.com (A.M.)

Abstract: In this study, a V@TiO₂ nanocomposite is examined for its ability to eliminate carcinogenic Rhodamine (Rh-B) dye from an aqueous medium. A simple ultrasonic method was used to produce the nanosorbent. In addition, V@TiO₂ was characterized using various techniques, including XRD, HRTEM, XPS, and FTIR. Batch mode studies were used to study the removal of Rh-B dye. In the presence of pH 9, the V@TiO₂ nanocomposite was able to remove Rh-B dye to its maximum extent. A correlation regression of 0.95 indicated that the Langmuir model was a better fit for dye adsorption. Moreover, the maximum adsorption capacity of the V@TiO₂ nanocomposite was determined to be 158.8 mg/g. According to the thermodynamic parameters, dye adsorption followed a pseudo-first-order model. Based on the results of the study, a V@TiO₂ nanocomposite can be reused for dye removal using ethanol.

Keywords: V@TiO₂ nanocomposite; Rh-B dye removal; removal mechanism; regeneration



Citation: Elamin, M.R.; Abdulkhair, B.Y.; Elamin, N.Y.; Ibnaouf, K.H.; Idriss, H.; Bakheit, R.; Modwi, A. Application of Synthesized Vanadium–Titanium Oxide Nanocomposite to Eliminate Rhodamine-B Dye from Aqueous Medium. *Molecules* **2023**, *28*, 176. <https://doi.org/10.3390/molecules28010176>

Academic Editors: Monika Wawrzekiewicz and Anna Wołowicz

Received: 1 December 2022

Revised: 18 December 2022

Accepted: 20 December 2022

Published: 25 December 2022



Copyright: © 2022 by the authors. Licensee MDPI, Basel, Switzerland. This article is an open access article distributed under the terms and conditions of the Creative Commons Attribution (CC BY) license (<https://creativecommons.org/licenses/by/4.0/>).

1. Introduction

Industrial wastewater contains artificial pigments that constitute an environmental risk; thus, toxic dyes should permanently be removed from the aquatic system [1]. Dumping colored wastewater into receiving waterways has become a severe environmental issue worldwide [2]. The release of wool, rug, pulp, sheet, and textile effluents frequently tint the collecting waters for kilometers in the direction of the source [3]. The color is visually unappealing and inhibits the passage of light into the water, lowering the effectiveness of photosynthesis in aquatic plants and negatively affecting their development [4]. The extensive use of dyes in the fabric, publishing, latex, beauty product, plastic, and leather sectors produces a massive volume of colored wastewater [5–7]. Rhodamine B has a comprehensive application, encompassing textiles, food, laser technology, biomarkers, molecular probes, sensitizers, electrochemical-luminescence, and solar panels [8]. Rhodamine B (Rh-B) dye is considered a skin-irritating agent, neurotoxic, chronically toxic to aquatic organisms, and carcinogenic to humans. [9]. Thus, purifying water bodies from Rhodamine B is an urgent task to protect the environment and human health. One of the most popular cationic water-soluble organic dyes is Rh-B [10]; it is toxic and lethal to aquatic environments [11]. The numerous procedures for decolorization are categorized as chemical, physical, and microbial techniques [12–14]. Physical treatments involve sorption, ozonation, and membrane processes [15]. While chemical procedures comprise oxidation,

precipitation/co-precipitation, and photochemical processes, biological techniques include aerobic decomposition, bacterial destruction, and biosorption [16]. Even though these approaches are successful, they have several drawbacks, including increased chemical consumption and sludge formation, and they are expensive [17].

Among all the dye treatment procedures, adsorption is reported to be efficient and economical [18]. Activated carbon is an efficient adsorbent for removing dyes from industrial sewage effluents; nevertheless, its cost limits its usage [19]. Alongside traditional adsorbents, various economical nonconventional adsorbents have been demonstrated to eliminate dyes efficiently [20]. For the removal of dyes, investigations, including the analysis of practical and inexpensive adsorbents produced from available resources, are increasingly relevant [21]. Employing nanotechnology to clean contaminated environments has shown to be advantageous, saving a lot and lowering pollution levels to tolerable levels [22–24]. Metallic nanoparticles and nanocomposites are regarded as potential adsorbents with high dye removal capability due to their sensitivity, permeability, and recyclability within each known sorbent [25,26]. Lately, metal-based nanocomposites such as MgO/TeSe, $(Y_2O_3)_n$ -ZnO, GO-TiO₂, Fly-Ash@Fe₃O₄, and Fe₂O₃-TiO₂-graphene have been used to eliminate various dyes from water systems [27–33]. Several proposals for nanoparticle production have involved mechanical, physiochemical, and biological procedures [34–36]. Furthermore, nanostructured and composite materials can be employed to capture or destroy dye contamination in an aqueous environment [37–39]. V-TiO₂ was utilized as the base material to synthesize triple composites and used mostly as a photocatalyst [40–42].

This research aimed to establish a straightforward method for producing V-TiO₂ nanomaterial. The synthesized V-TiO₂ will be analyzed by physical means and introduced as a practical, environmentally friendly, and inexpensive composite to get rid of the coloring dyes from water.

2. Experimental Section

2.1. Fabrication of V@TiO₂ Sorbent

For the V-TiO₂ sorbent, 0.0338 moles of TiO₂ nanoparticles (Sigma Aldrich) were dispersed in 0.12 L isopropanol solvent using an ultrasonic bath for 20.0 min. Then, 0.00165 moles of V₂O₅ were added to the milky TiO₂ solution, and the mixture was sonicated for a further 40.0 min with vigorous stirring (550 rpm). After the mixtures were blended, they were heated for 20 h at 90 °C in an electric dry oven, and the resulting nanoparticles were ground before being calcined. The greenish-white powders were annealed for 2 h at 145 °C.

2.2. Sorbent Characteristics

The structural properties of the as-synthesized sample were investigated by X-ray diffraction (XRD) utilizing a Rigaku diffractometer operated with Cu K radiation ($\lambda = 0.15406$ nm) at 40 kV and 40 mA. Fourier transform infrared (FT-IR) spectra were acquired with the KBr pellet (400 to 4000 cm⁻¹) on a Thermo Scientific Nicolet 380 Fourier transform spectrometer. Using a JEM-2100 high-resolution transmission electron microscope (TEM), the microscopic characteristics of the materials were studied. X-ray photoelectron spectroscopy (XPS) was utilized to investigate surface chemistry using an RBD upgraded PHI-5000C ESCA system (Perkin Elmer) with Al K radiation ($h\nu = 1486.6$ eV).

2.3. Rh-B Sorption Studies

The batch test protocol was employed to investigate the Rh-B dye adsorption onto the V@TiO₂ nanocomposite. In 0.025 L small bottles, 5 to 100 ppm concentrations of Rh-B dye in distilled water were mixed with 10 mg of the nanocomposite. The mixture solution was constantly agitated for 20 h. Following the establishment of equilibrium with the aqueous phase, the nanocomposite was isolated by filtering, and Rh-B dye concentrations were measured using a UV-vis spectrophotometer. The amount of adsorbed Rh-B dye at any

given time (in minutes) and adsorption equilibrium magnitudes Q_t and Q_e (mg/g) were calculated using the same equation (Equation (1)):

$$Q_t = V(C_0 - C_t)/m \quad (1)$$

where V is the volume of the solution in liters; C_0 , C_e , and C_t are the starting concentration, equilibrium concentration, and concentration of the Rh-B dye in solution, respectively, in milligrams per liter; and m is the mass of the adsorbent (g). The contact times data were used to investigate the Rh-B sorption via the pseudo-first-order, and pseudo-second-order models (PSFOM, PSSOM) as expressed in equations 2 and 3, respectively. Also, the sorption control mechanism was studied utilizing the liquid film and the intraparticle diffusion models (IDM and LDM) presented by Equations (4) and (5) [43]:

$$q_t = q_e \left(1 - \exp^{-k_1 \cdot t}\right) \quad (2)$$

$$q_t = \frac{k_2 \cdot q_e^2 \cdot t}{1 + k_2 \cdot q_e \cdot t} \quad (3)$$

$$\ln(1 - F) = -K_{LF} \cdot t \quad (4)$$

$$q_t = K_{IP} \cdot t^{\frac{1}{2}} + C_i \quad (5)$$

where q_e (mg g⁻¹) represents q_t at equilibrium and k_1 (min⁻¹) and k_2 (g mg⁻¹ min⁻¹) are the rate adsorption constants for the PSFO and PSSO models, which have been calculated from the slope and intercept values, respectively. The LFD and IPDM constants were represented as K_{IP} (mg g⁻¹ min^{-0.5}) and K_{LF} (min⁻¹), and both were computed from their slope values. C_i (mg g⁻¹) is a boundary-layer-thickness factor [44].

2.4. pH Point of Zero Charges Experiment

In each flask, with a pH ranging from 1 to 12, ten milligrams of V@TiO₂ nanocomposite and ten milliliters of a 0.1 mole/L sodium chloride (NaCl) solution were added. A trace amount of hydrochloric acid or sodium hydroxide was incorporated into the solution in order to bring about a change in the pH. In order to achieve equilibrium, these bottles were left on a multi-stirrer at room temperature for exactly one hour; then, the pH levels of the solutions were measured. The point zero charges were found by comparing the initial and final pH values against the original pH graph.

3. Results and Discussions

3.1. XRD Analysis of V@TiO₂ Nanocomposite

X-ray diffraction (XRD) examination was conducted to verify the produced V@TiO₂ nanocomposite. Figure 1 depicts XRD data from generated samples pertaining to the structural properties of the V@TiO₂ nanocomposite. Peaks of phase obtained at $2\theta = 27.51, 36.19, 44.19,$ and 54.42 are consistent with rutile phase (110), (101), (111), and (211), respectively. On the other hand, the appearance of diffraction peaks at 41.42° and 56.66° corresponds to orthorhombic phase planes (020) and (012) of V₂O₅, which is consistent with JCPDS Card No. 01-0359 [45]. By means of the Debye–Scherer equation [46], the average crystal size of the V@TiO₂ nanocomposite was determined to be 33.83 nm, with a d-spacing of 3.236 Å.

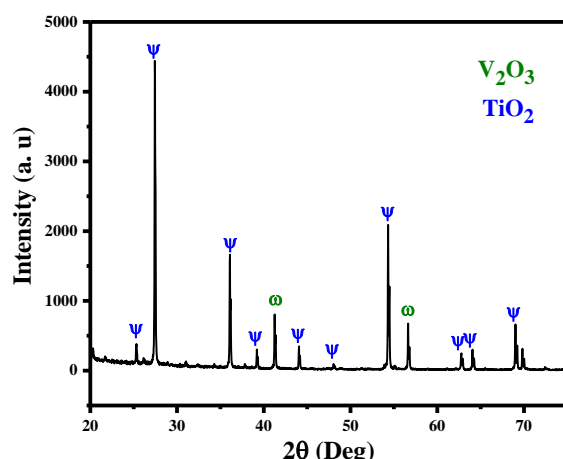


Figure 1. XRD of the fabricated V@TiO₂ nanocomposite.

3.1.1. Morphological Observations

The TEM images of the V@TiO₂ sorbent at different magnifications confirmed the morphology and indicated the elemental distribution, as shown in Figure 2a–c. The semi-spherical form of the TiO₂ nanoparticles is seen clinging to the V₂O₅ nanomaterials, as shown in the TEM pictures. The elemental distribution of V, Ti, and O in the synthesized nanomaterials is characterized by means of EDX spectra (Figure 2d). The EDX analysis sheds light on the stoichiometry of oxygen, vanadium, and titanium, as well as the proportions of these elements and the actual integration of V₂O₅ into the TiO₂ lattice. The transmission electron microscope (TEM) gave an estimate of 30–100 nm for the typical particle size of the sorbent. The value, however, was comparable to the crystallite size determined by XRD.

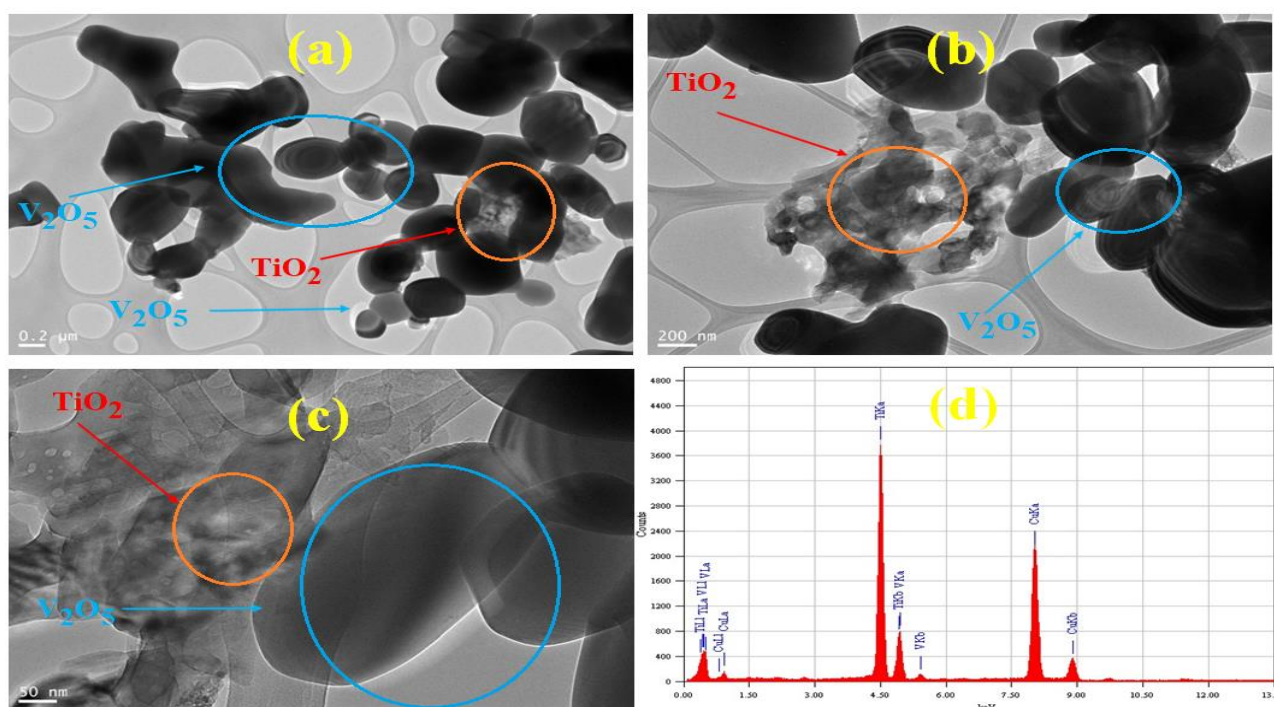


Figure 2. (a–c) TEM images at different magnifications and (d) EDX of the V@TiO₂ nanocomposite.

3.1.2. XPS of V@TiO₂ Nanocomposite

Figure 3a–c depict O1s, Ti 2p, and V2p core-level spectra of the V₂O₅–TiO₂ samples. The O1s peak fit into two Gaussian peaks at 529.8 eV, which arose from the lattice O

(Ti–O–Ti) and surface-absorbed hydroxyl groups of Ti–OH (Figure 3a) [47]. Due to the self-orbital coupling effect, the Ti 2p peak was subdivided into Ti 2p_{3/2} (458.3 eV) and Ti 2p_{1/2} (464.1 eV), as shown in Figure 3c. They were symmetrical with a normal Gaussian peak shape, indicating that Ti⁴⁺ was predominantly present in the undoped sample. Due to the influence of the O1s satellite peak, only the V 2p_{3/2} peak was displayed in the current experiment. The V doped in the TiO₂ nanoparticles (Figure 3d) consisted of two chemical states, V⁵⁺ and V⁴⁺, with energies of 514.9 and 527.33 eV, respectively. The literature [48] indicates that V dopants can exist in surficial VO²⁺, surficial V₂O₅ islands, interstitial, and replacement V ions. In light of the XRD and TEM analyses, as well as the fact that V doping can result in the O1s peak shifting, it is plausible to assume that the V ions existed in a substituted form and not as the V₂O₅ isolated phase, as suggested by the literature [49].

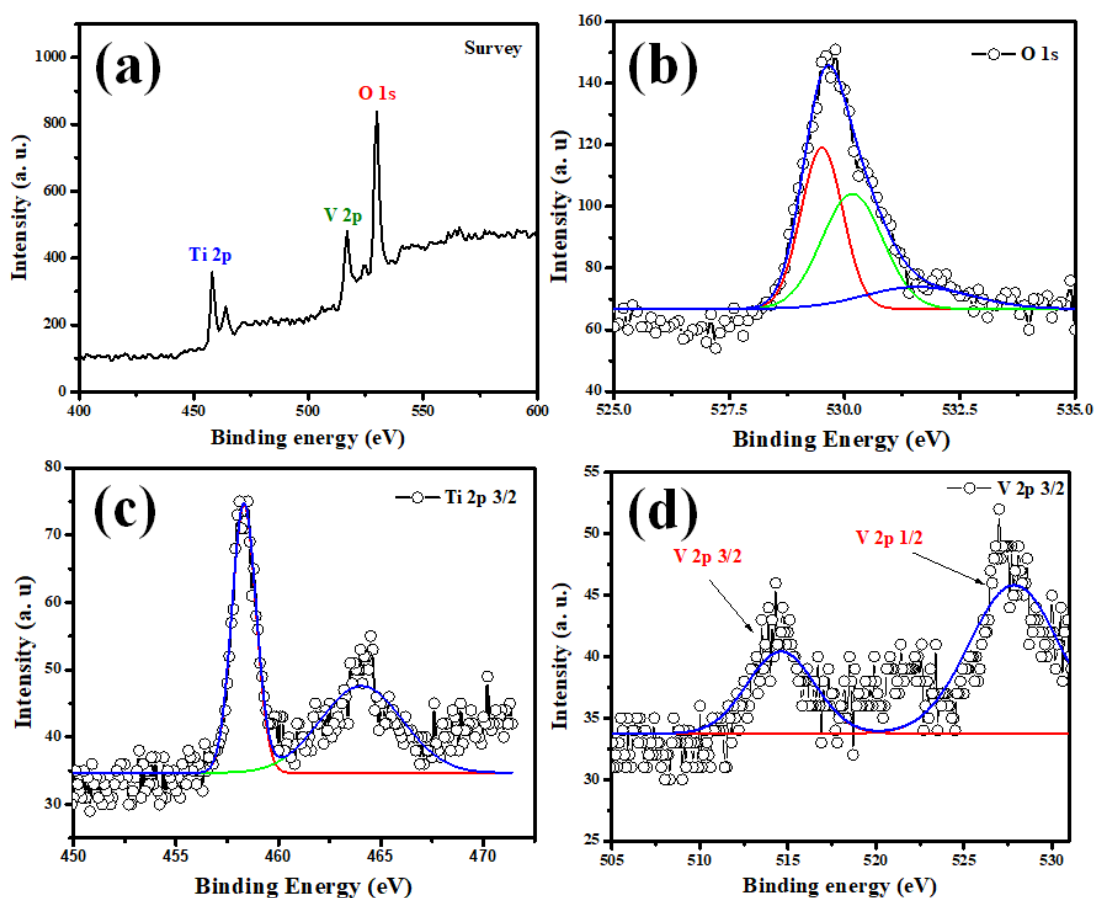


Figure 3. Extraordinary resolution XPS spectra of (a) Survey (b) O1s, (c) Ti 2p 3/2, and (d) V 2p 3/2 of V₂O₅-TiO₂ nanohybrid.

Usually, due to the similar radii of V⁴⁺ and Ti⁴⁺ species, V⁴⁺ ions can typically only integrate into the TiO₂ lattice by substituting Ti⁴⁺ ions. Therefore, the Ti–O–V bond, which results in oxygen vacancy and a high electron production capability, is formed by sharing the oxygen atoms of the V⁴⁺ ions in the TiO₂ lattice. Furthermore, the presence of more V⁴⁺ ions leads to the creation of more O₂ radicals, the most powerful oxidizing species in photocatalysis [50,51]. As a result, the existence of V⁴⁺ contributes significantly to the improvement of photocatalytic activity [52].

3.1.3. pHzc of V@TiO₂ Nanocomposite

The pH of the point of zero charge (pH_{zc}) of the V@TiO₂ nanocomposite was evaluated using the pH drift method to completely comprehend the pH effect on the adsorptive removal of dye pollution from an aqueous medium. According to the obtained results, the

pHZPC value of the V@TiO₂ nanocomposite was 4.2. At this pH (pH_{ZC} = 4.2), the surface charge on the V@TiO₂ nanocomposite is zero, whereas the surface charge is positive at pH values less than 4.2 and negative at pH values greater than the pH_{ZPC} (Figure 4). The influence of pH on Rh-B dye removal is a significant factor for the adsorption technique, as it modifies not only the active sites on the V@TiO₂ surface of the adsorbent that are capable of Rh-B dye bonding, but also the solubility of Rh-B dye in the aqueous solution.

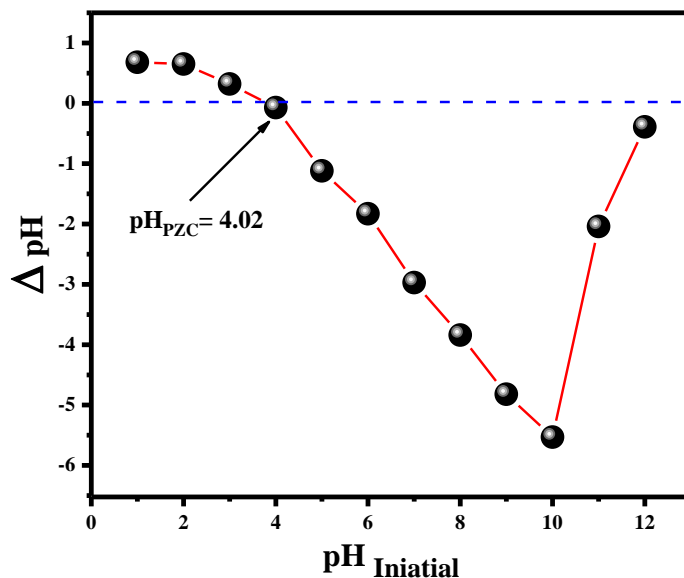


Figure 4. pH zero charge of the V@TiO₂ nanocomposite.

3.1.4. Surface Characteristics of the V@TiO₂ Nanocomposite

From the surface property investigation, the isotherm and pore size distribution of the manufactured V@TiO₂ nanocomposite are depicted in Figure 5a. The resulting isotherm is of class IV with H1 hysteresis loops, which seem to be characteristic of nanostructured and mesoporous materials [53,54]. Figure 5b shows a BET surface area of 16 m²/g and a pore volume of 0.018 cc/g, along with a pore size distribution with a median of roughly 27.6 nm.

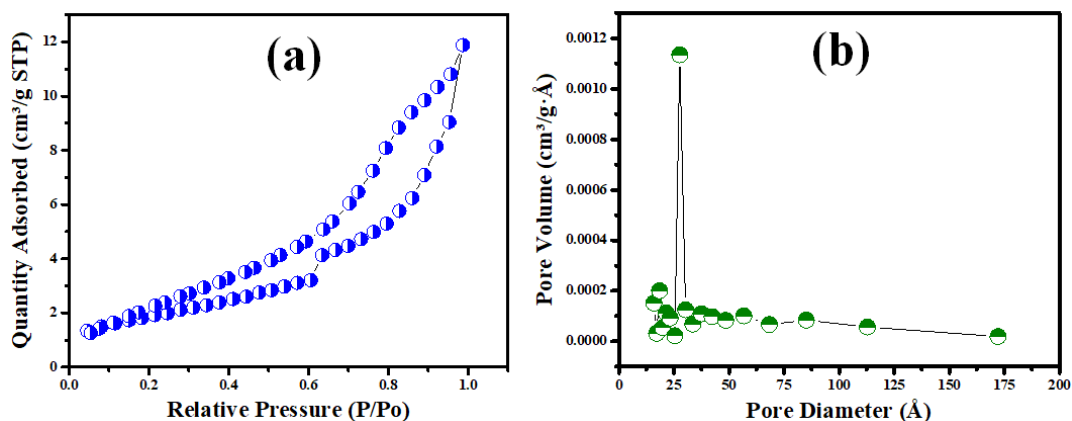


Figure 5. (a) The nitrogen adsorption–desorption isotherm and (b) the pore distribution of the V@TiO₂ nanocomposite.

3.2. Adsorption of Rd-B by V@TiO₂ Sorbent

Figure 6a depicts the effect of contact duration on Rh-B dye sorption on V@TiO₂, with experimental q_t values of 138 mg g⁻¹ and adsorption equilibrium points of 4.0 h. It is worth mentioning that nearly 95% of these uptakes occurred during the first 60 min of

interaction. In addition, the impact of the concentrations of Rh-B on sorption by V@TiO₂ was tested. Figure 6b illustrates that the q_t value increased proportionally up to 75 mg L⁻¹, after which the inflation occurred, indicating the suitability of a 1:4 sorbent solution ratio up to 75 mg L⁻¹. Typically, q_t values of 133.4 mg g⁻¹ from 100 mg L⁻¹ Rh-B solutions imply the applicability of the V@TiO₂ for treating industrial effluents with high pollutant concentrations. Additionally, the semi-complete Rh-B dye removal by V@TiO₂ from the 10 mg L⁻¹ solutions demonstrates its effectiveness in treating contaminated water resources. Furthermore, the decrease of q_t values from the same concentrations as the temperature increased showed the exothermic nature of removing Rh-B dye by a V@TiO₂ sorbent.

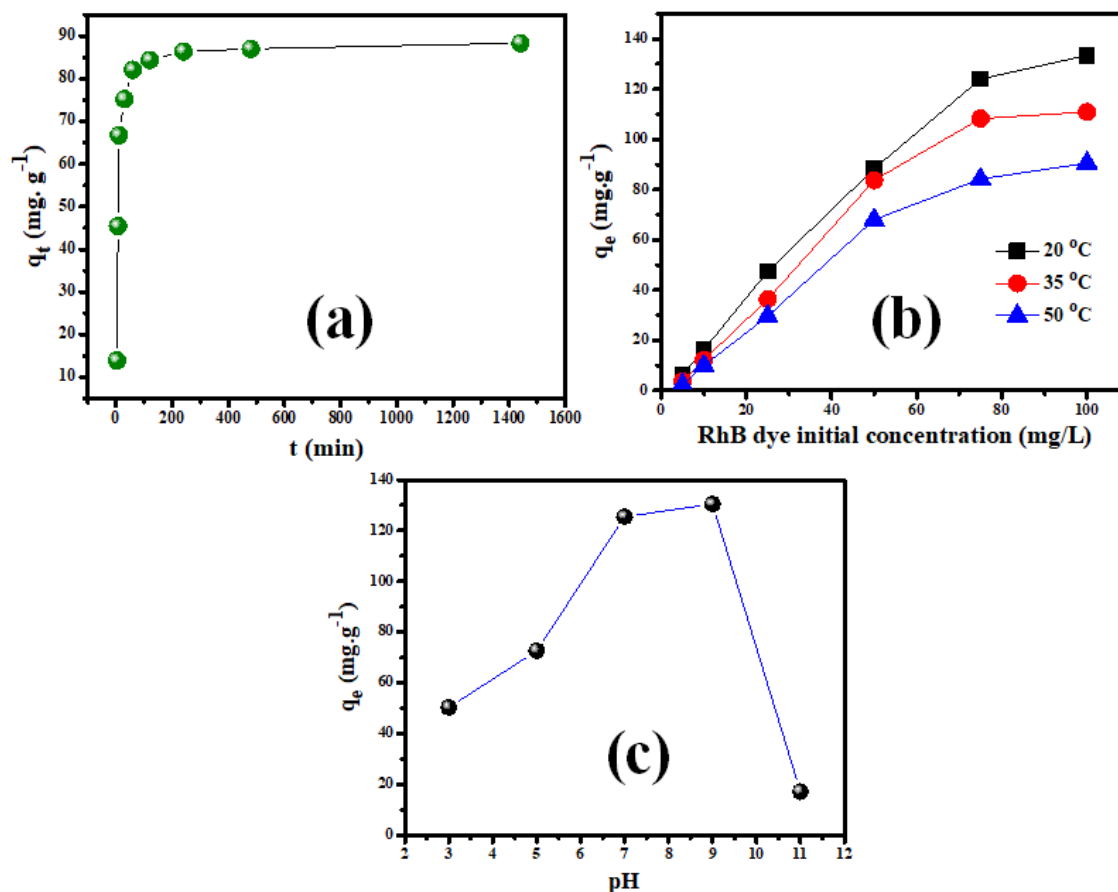


Figure 6. (a) The contact time study for the adsorption of Rh-B dye on the synthesized V@TiO₂, (b) the influence of a solution's pH on Rh-B dye sorption, (b) the impact of feeding concentration on the Rh-B sorption on V@TiO₂ at 20 °C, 35 °C, and 50 °C for (a) Rh-B dye, and (c) The zero-charge investigation of V@TiO₂.

Furthermore, the pH impact on Rh-B adsorption on V@TiO₂ was evaluated (Figure 6c). The obtained results show the suitability of mild alkaline media for removing Rh-B dye. The decrease in sorption capacity for V@TiO₂ in strongly acidic media is probably due to the protonation of oxygen atoms in the nanocomposite and/or turning part of the oxides into soluble salts. On the other hand, the hydroxyl groups in strong alkaline media may compete with Rh-B dye for sorbent sites and/or repulse it away from the V@TiO₂ surface [55,56].

3.2.1. Adsorption Kinetics

The linear regression plots of the PSFOM, PSSOM, IDM, and LDM for Rh-B dye sorption on V@TiO₂ are illustrated in Figure 7. The k_1 , k_2 , K_{IDM} , and K_{LDM} values gathered in Table 1 were computed utilizing the extracted regression parameters (slope and intercept) [43,57]. The obtained results revealed that Rh-B sorption on V@TiO₂ fit the

PSFOM model, which may explain their relatively short-time equilibrium. Further, the investigation of the rate-control step showed that the intraparticle diffusion step controlled the adsorption of Rh-B onto the V@TiO₂ surface. These findings indicate that Rh-B dye has a higher affinity toward the V@TiO₂ surface and imply fast pore-diffusion during the Rh-B dye removal by V@TiO₂ [58].

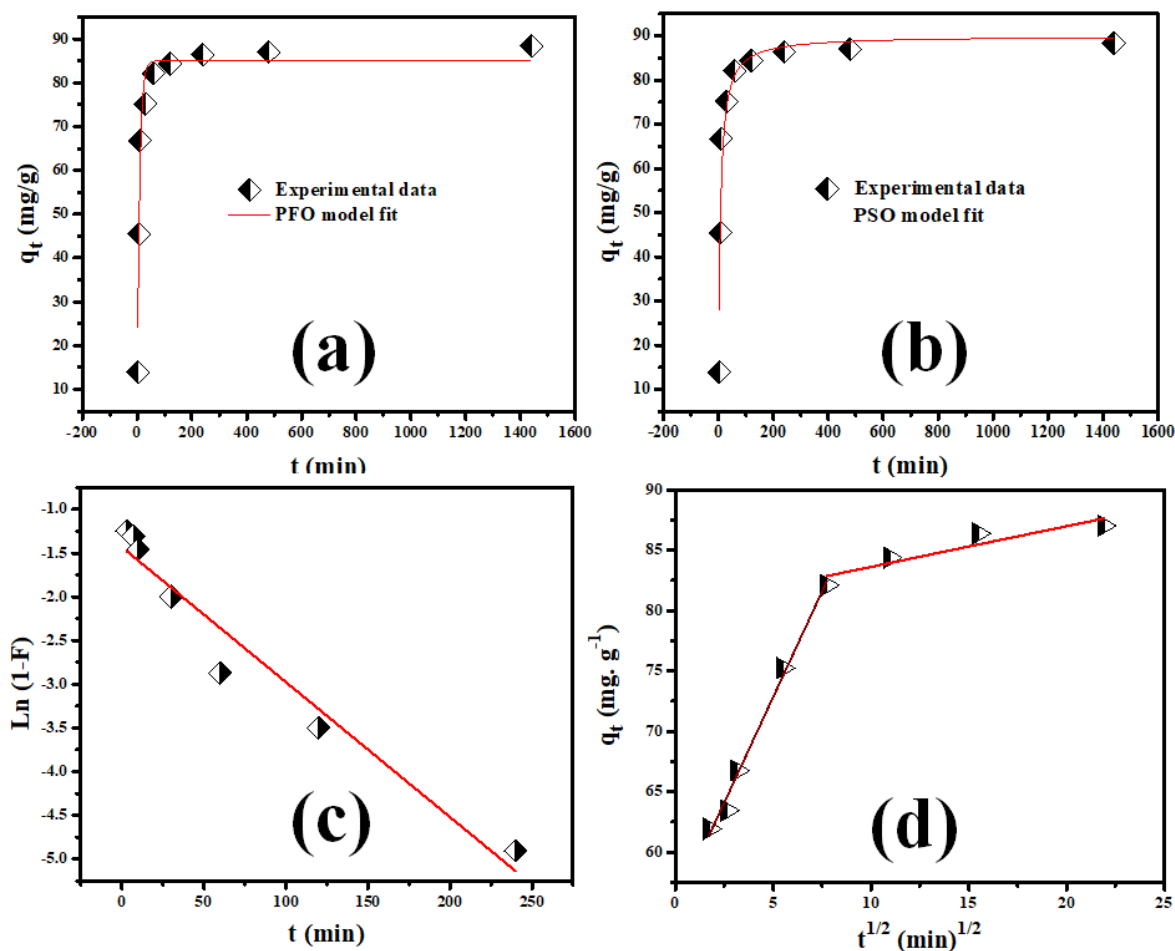


Figure 7. (a,b) The PSFO and PSSO sorption rate order investigations for Rh-B sorption on the V@TiO₂ nanocomposite; (c,d) LFD and IPD sorption mechanism investigations for Rh-B sorption on the V@TiO₂ nanocomposite.

Table 1. The kinetic parameters for Rh-B adsorption on the V@TiO₂ nanocomposite from 50 mg L⁻¹ pollutant solution.

Adsorption Kinetic						
Adsorption Rate Order						
q_e exp. (mg g ⁻¹)	PSFO			PSSO		
	q_e cal. (mg g ⁻¹)	R ²	k_1	q_e cal. (mg g ⁻¹)	R ²	k_2
88.367	88.7	0.947	0.114	90.000	0.927	0.002
Adsorption mechanism						
IPDM			LFDM			
	K_{IP} (mg g ⁻¹ min ^{0.5})	C (mg g ⁻¹)	R ²	K_{LF} (min ⁻¹)	R ²	
Stage 1	3.4950	55.38	0.9959	0.015	0.956	
Stage 2	0.3369	80.256	0.9306			

3.2.2. Adsorption Isotherms

The Langmuir and Freundlich models (LIM and FIM) were the most used isotherm models for describing adsorption processes. Both linearized models (Equations (6) and (7)) were utilized to analyze Rh-B sorption on synthesized V@TiO₂.

$$q_e = \left(\frac{K_L q_m C_e}{1 + q_m C_e} \right) \quad (6)$$

$$q_e = K_F \cdot C_e^{\frac{1}{n}} \quad (7)$$

In these equations, C_e (mg L⁻¹) is the equilibrium solution concentration, q_m is the computed maximum sorption capacity, $1/n$ is the Freundlich adsorption intensity, and K_L and K_F are the LIM and FIM constants, respectively [59]. The linear fits of LIM and FIM studies of Rh-B sorption on synthesized V@TiO₂ are shown in Figure 8. Better fitting to LIM was observed in the data presented in Table 2. The Rh-B sorption showed preferential sorption, as indicated by the $1/n$ value below unity, which was also consistent with its PFOM agreement [60–62].

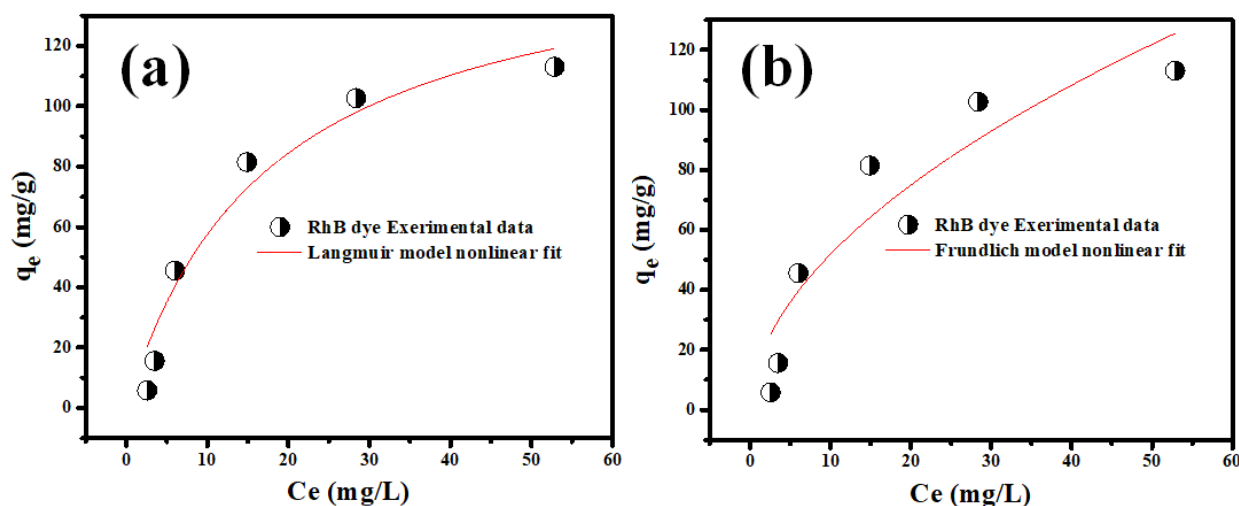


Figure 8. The (a) LIM and (b) FIM investigations for the adsorption of Rh-B on the synthesized V₂O₅@TiO₂ at 20 °C.

Table 2. Removal parameters of the V@TiO₂ sorbent compared with the diverse Rh-B dye adsorbent nanomaterials.

Nanomaterials	Adsorption Capacity (mg g ⁻¹)	References
Halloysite HU	8.37	[63]
alpha alumina (α -Al ₂ O ₃)	52.0	[64]
L-Asp capped Fe ₃ O ₄ NPs	7.7	[65]
Magnetic ZnFe ₂ O ₄	12.1	[66]
MWCNT-COOH	42.68	[67]
Humic acid functionalized MNPs	161.8	[68]
Sodium montmorillonite	42.19	[69]
Lignocellulose	82.34	[70]
NiO nanoparticles	111	[71]
NiZnAl-LDH nano-sheets	97.09	[72]
V@TiO ₂ nanocompositie	158.8	This paper

As shown in Table 2, the performance of the V@TiO₂ nanocomposite in adsorbing Rh-B dye has been further evaluated and compared to that of other adsorbents that have been reported in the literature. First, the equilibrium time for the V@TiO₂ nanocomposite is

shorter. These obtained results show that the Rh-B dye leaves the aqueous solution quickly. Further, the V@TiO₂ nanocomposite has a more significant adsorption capacity than the other nanostructures, i.e., 158.8 mg/g compared to 7–161 mg/g, as documented in Table 2.

3.2.3. Adsorption Thermodynamics

The thermodynamics of Rh-B removal by the V@TiO₂ were inspected. The slope and intercept extracted from the plot of Equation (8) (Figure 9) were utilized in computing the enthalpy and entropy (ΔS° and ΔH°). The Gibbs free energy (ΔG°) was obtained by applying the ΔS° and ΔH° values in Equation (9). The ideal gas constant (R) was used as 0.0081345 kJ mol⁻¹ for calculating these parameters, and the findings are summarized in Table 3.

$$\ln K_c = \frac{\Delta H^{\circ}}{RT} + \frac{\Delta S^{\circ}}{R} \quad (8)$$

$$\Delta G^{\circ} = \Delta H^{\circ} - T \Delta S^{\circ} \quad (9)$$

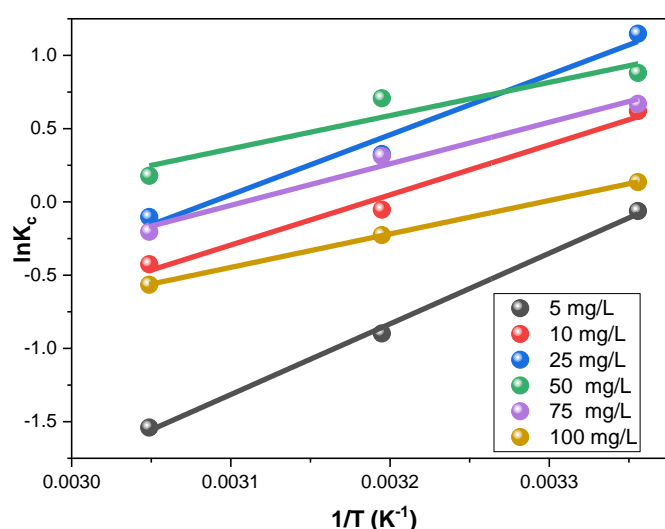


Figure 9. Thermodynamic study of the sorption of Rh-B on the synthesized V@TiO₂ at 298, 313, and 328 °K.

Table 3. The isotherms and thermodynamic findings for the Rh-B sorption on the V@TiO₂ nanocomposite.

Adsorption Isotherms						
Langmuir			Freundlich			
R ²	K _L (L mg ⁻¹)	q _m (mg g ⁻¹)	R ²	K _f (L mg ⁻¹)	n ⁻¹ (a.u.)	
0.952	0.056	158.8	0.880	0.536	0.065	
Thermodynamic parameters						
Fed conc. (mg L ⁻¹)	ΔH° (kJmol ⁻¹)	ΔS° (kJmol ⁻¹)	ΔG° (kJmol ⁻¹) 298 K	ΔG° (kJmol ⁻¹) 313 K	ΔG° (kJmol ⁻¹) 328 K	
10	-28.450	-0.091	-1.439	-0.079	1.280	
25	-34.026	-0.105	-2.714	-1.138	chem1.280	
50	-18.856	-0.055	-2.335	-1.503	-0.672	
75	-23.573	-0.073	-1.739	-0.640	0.460	
100	-18.979	-0.063	-0.339	0.599	1.537	

Table 3 shows that Rh-B sorption possessed negative ΔG° values, indicating the sorption's spontaneity and exothermic nature. Also, the negative ΔH° values corroborate that V@TiO₂ removed the Rh-B dye via a physisorption process [73–77].

3.3. Rh-B Dye Adsorption Mechanism

Several variables, such as the functional group of adsorbents, the pH of a solution, the surface charge on the particles, the porosity, and the nature of the adsorbate, can affect the adsorption process. Rh-B dye was adsorbed on the V@TiO₂ nanocomposite surface in this study. Point zero charges (surface charge) and FTIR (functional groups) that existed on the V@TiO₂ sorbent could explain the likely mechanism of the adsorption process. Hydrogen bonding and electrostatic interactions might have contributed to the adsorption of the Rh-B dye (Figure 10a). In Figure 10a of the FTIR spectrum, the absorption peak at 2309 cm⁻¹ due to C–N stretching vibrations that appeared after the adsorption of Rh-B dye demonstrates its role in the adsorption of dye molecules. Due to the presence of C–H and C=C functional groups in the spectra of adsorbed Rh-B dye, the absorption band between 1539.58 and 1448 cm⁻¹ was observed. The narrow peak between 1000 and 900 cm⁻¹ is attributable to the C–H bond, which indicates their participation in the elimination of Rh-B dye. A prominent broad peak at 521 cm⁻¹, which shifted lower to 472 cm⁻¹, correlates to V@TiO₂ nanocomposite stretching; FTIR of the dye-loaded V@TiO₂ nanocomposite revealed a considerable drop in the peak, indicating its significance in the elimination of Rh-B dye from an aqueous solution.

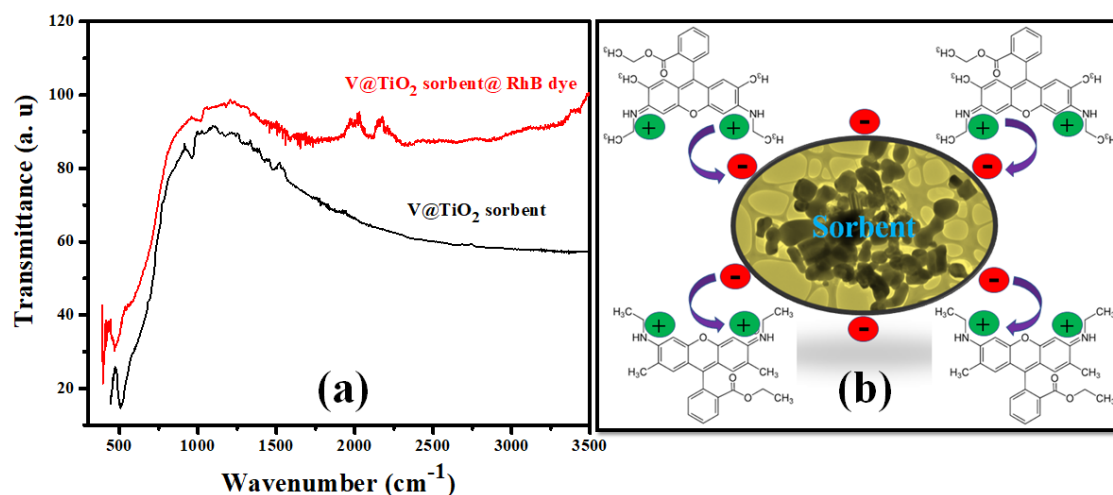


Figure 10. (a) FTIR spectra of the V@TiO₂ nanocomposite and Rh-B @ V@TiO₂ nanocomposite; (b) the suggested removal mechanism of Rh-B dye by the V@TiO₂ nanocomposite.

The pH_{zpc} study determined that the pH_{zpc} exists at a pH of 4.2, above which the surface of V@TiO₂ is negatively charged, which may increase the sorption by withdrawing the positive N⁺–(CH₃)₂ group on Rh-B (Figure 10a); this hypothesis indicates high participation of electrostatic attractions in Rh-B removal by V@TiO₂. Furthermore, the adsorption of Rh-B dye on the surface of the V@TiO₂ sorbent is also the result of interactions involving H–H bonding and dipole–dipole interactions. In addition, the isothermal studies demonstrate that the multilayer adsorption of the Rh-B molecules is physical sorption; this result is in line with the ΔH^o values less than 80 kJmol⁻¹. Figure 10b depicts the subsequent adsorption of Rh-B dye molecules onto the V@TiO₂ sorbent. Rh-B dye is attracted to the nanocomposites via hydrogen bonds and electrostatic interactions.

3.4. V@TiO₂ Nanomaterials Regeneration

The regeneration of V@TiO₂ nanomaterials was studied by removing the Rh-B dye using absolute ethanol. During the regeneration process, ethanol was used as the desorption agent (Figure 11). The rapid discoloration of absolute ethanol filtrate confirmed Rh-B dye desorption from the V@TiO₂ sorbent. The sorbent was re-immersed in a freshly produced Rh-B dye solution with the same concentration and volume (5 mg/L, 75 mL). A total of five repetitions of this step were performed. Figure 11 illustrates the effectiveness of Rh-B dye

desorption by ethanol from the V@TiO₂ sorbent. The efficacy of the V@TiO₂ nanocomposite to remove dyes decreased with each desorption cycle.

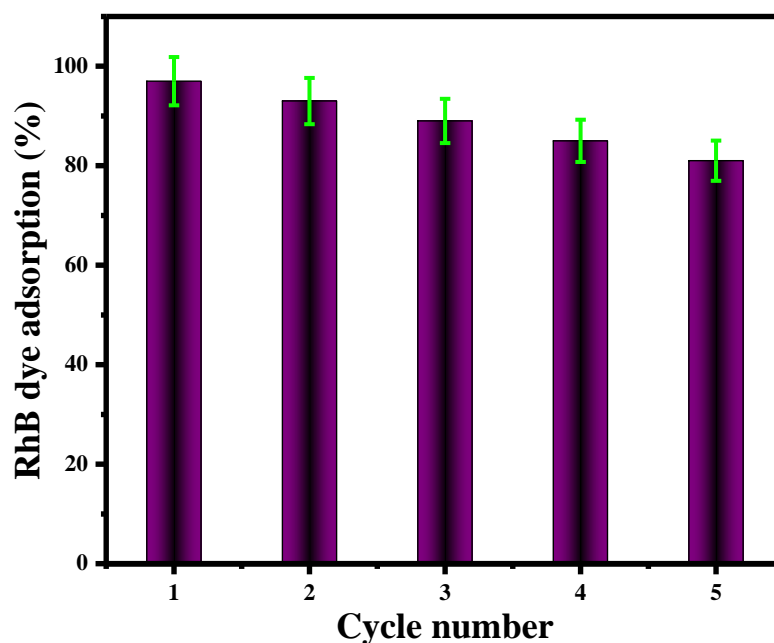


Figure 11. V@TiO₂ nanomaterial regeneration.

4. Conclusions

Nanostructured V@TiO₂ is synthesized from metal oxide using ultrasonic synthesis techniques. A study of the adsorption properties of Rh-B dye on V@TiO₂ was conducted. According to XRD, the V@TiO₂ nanomaterials had a crystal size of 33.83 nm. In aqueous media, the nanosorbent of V@TiO₂ was demonstrated to be capable of eliminating Rh-B dye molecules with a maximum adsorption capacity of 158.8 mg/g. Furthermore, the thermodynamic analysis showed that such reactions were highly spontaneous and endothermic. The Langmuir technique emphasized the adsorption monolayer. As a result, the adsorption kinetic could be fitted with a pseudo-first-order reaction model. Additionally, 100% ethanol was chosen as the best selective desorption eluent for reusing the adsorbent. Hence, the regeneration of V@TiO₂ sorbent is a cost-effective method for treating effluents from the textile industry.

Author Contributions: A.M.: conceptualization, writing—original draft, preparation; M.R.E.: supervision, writing, review of the final version; B.Y.A.: writing, review of the final version; N.Y.E.: validation, writing, review; K.H.I.: writing, review; R.B. and H.I.: review. All authors have read and agreed to the published version of the manuscript.

Funding: The Deanship of Scientific Research at Imam Mohammad Ibn Saud Islamic University funded this work through Research Group no. RG-21-09-74.

Institutional Review Board Statement: Not applicable.

Acknowledgments: The authors extend their appreciation to the Deanship of Scientific Research at Imam Mohammad Ibn Saud Islamic University for funding this work.

Conflicts of Interest: The authors declare that they have no known competing financial interests or personal relationships that could have appeared to influence the work reported in this paper.

References

1. Tkaczyk, A.; Mitrowska, K.; Posyniak, A. Synthetic organic dyes as contaminants of the aquatic environment and their implications for ecosystems: A review. *Sci. Total Environ.* **2020**, *717*, 137222. [[CrossRef](#)] [[PubMed](#)]
2. Ehalt Macedo, H.; Lehner, B.; Nicell, J.; Grill, G.; Li, J.; Limtong, A.; Shakya, R. Distribution and characteristics of wastewater treatment plants within the global river network. *Earth Syst. Sci. Data* **2022**, *14*, 559–577. [[CrossRef](#)]
3. Rápó, E.; Tonk, S. Factors affecting synthetic dye adsorption; desorption studies: A review of results from the last five years (2017–2021). *Molecules* **2021**, *26*, 5419. [[CrossRef](#)] [[PubMed](#)]
4. Peng, X.; Lin, Q.; Liu, B.; Huang, S.; Yan, W.; Zhang, L.; Ge, F.; Zhang, Y.; Wu, Z. Effect of submerged plant coverage on phytoplankton community dynamics and photosynthetic activity in situ. *J. Environ. Manag.* **2022**, *301*, 113822. [[CrossRef](#)] [[PubMed](#)]
5. Mugdha, A.; Usha, M. Enzymatic treatment of wastewater containing dyestuffs using different delivery systems. *Sci. Rev. Chem. Commun.* **2012**, *2*, 31–40.
6. Pang, Y.L.; Abdullah, A.Z. Current status of textile industry wastewater management and research progress in Malaysia: A review. *Clean–Soil Air Water* **2013**, *41*, 751–764. [[CrossRef](#)]
7. Gürses, A.; Açıkyıldız, M.; Güneş, K.; Gürses, M.S. Dyes and pigments: Their structure and properties. In *Dyes and Pigments*; Springer: Berlin/Heidelberg, Germany, 2016; pp. 13–29.
8. Butman, M.F.; Gushchin, A.A.; Ovchinnikov, N.L.; Gusev, G.I.; Zinenko, N.V.; Karamysheva, S.P.; Krämer, K.W. Synergistic effect of dielectric barrier discharge plasma and TiO₂-pillared montmorillonite on the degradation of rhodamine B in an aqueous solution. *Catalysts* **2020**, *10*, 359. [[CrossRef](#)]
9. Dire, D.J.; Wilkinson, J.A. Acute exposure to rhodamine B. *J. Toxicol. Clin. Toxicol.* **1987**, *25*, 603–607. [[CrossRef](#)]
10. Ali Khan, M.; Siddiqui, M.R.; Otero, M.; Alshareef, S.A.; Rafatullah, M. Removal of rhodamine b from water using a solvent impregnated polymeric dowex 5wx8 resin: Statistical optimization and batch adsorption studies. *Polymers* **2020**, *12*, 500. [[CrossRef](#)]
11. Wabaidur, S.M.; Khan, M.A.; Siddiqui, M.R.; Alothman, Z.A.; Al-Ghamdi, M.; Al-Sohami, H. Dodecyl sulfate chain anchored bio-char to sequester triaryl methane dyes: Equilibrium, kinetics, and adsorption mechanism. *Desal. Water Treat* **2017**, *67*, 357–370. [[CrossRef](#)]
12. Bhatia, D.; Sharma, N.R.; Singh, J.; Kanwar, R.S. Biological methods for textile dye removal from wastewater: A review. *Crit. Rev. Environ. Sci. Technol.* **2017**, *47*, 1836–1876. [[CrossRef](#)]
13. Hao, O.J.; Kim, H.; Chiang, P.-C. Decolorization of wastewater. *Crit. Rev. Environ. Sci. Technol.* **2000**, *30*, 449–505. [[CrossRef](#)]
14. Zouari, N. Decolorization of olive oil mill effluent by physical and chemical treatment prior to anaerobic digestion. *J. Chem. Technol. Biotechnol. Int. Res. Process Environ. AND Clean Technol.* **1998**, *73*, 297–303. [[CrossRef](#)]
15. Muhamad, M.S.; Salim, M.R.; Lau, W.J.; Yusop, Z. A review on bisphenol A occurrences, health effects and treatment process via membrane technology for drinking water. *Environ. Sci. Pollut. Res.* **2016**, *23*, 11549–11567. [[CrossRef](#)] [[PubMed](#)]
16. Akcil, A.; Erust, C.; Ozdemiroglu, S.; Fonti, V.; Beolchini, F. A review of approaches and techniques used in aquatic contaminated sediments: Metal removal and stabilization by chemical and biotechnological processes. *J. Clean. Prod.* **2015**, *86*, 24–36. [[CrossRef](#)]
17. Rajasulochana, P.; Preethy, V. Comparison on efficiency of various techniques in treatment of waste and sewage water—A comprehensive review. *Resour. Effic. Technol.* **2016**, *2*, 175–184. [[CrossRef](#)]
18. Jain, R.; Mathur, M.; Sikarwar, S.; Mittal, A. Removal of the hazardous dye rhodamine B through photocatalytic and adsorption treatments. *J. Environ. Manag.* **2007**, *85*, 956–964. [[CrossRef](#)]
19. Bakar, N.A.; Othman, N.; Yunus, Z.M.; Altowayti, W.A.H.; Tahir, M.; Fitriani, N.; Mohd-Salleh, S.N.A. An insight review of lignocellulosic materials as activated carbon precursor for textile wastewater treatment. *Environ. Technol. Innov.* **2021**, *22*, 101445. [[CrossRef](#)]
20. Crini, G.; Lichtfouse, E.; Wilson, L.D.; Morin-Crini, N. Conventional and non-conventional adsorbents for wastewater treatment. *Environ. Chem. Lett.* **2019**, *17*, 195–213. [[CrossRef](#)]
21. Adegoke, K.A.; Bello, O.S. Dye sequestration using agricultural wastes as adsorbents. *Water Resour. Ind.* **2015**, *12*, 8–24. [[CrossRef](#)]
22. Modwi, A.; Khezami, L.; Ghoniem, M.; Nguyen-Tri, P.; Baaloudj, O.; Guesmi, A.; AlGethami, F.; Amer, M.; Assadi, A. Superior removal of dyes by mesoporous MgO/g-C₃N₄ fabricated through ultrasound method: Adsorption mechanism and process modeling. *Environ. Res.* **2022**, *205*, 112543. [[CrossRef](#)] [[PubMed](#)]
23. Aissa, B.; Khezami, L.; Taha, K.; Elamin, N.; Mustafa, B.; Al-Ayed, A.; Modwi, A. Yttrium oxide-doped ZnO for effective adsorption of basic fuchsin dye: Equilibrium, kinetics, and mechanism studies. *Int. J. Environ. Sci. Technol.* **2022**, *9*, 9901–9914. [[CrossRef](#)]
24. Kerrami, A.; Khezami, L.; Bououdina, M.; Mahtout, L.; Modwi, A.; Rabhi, S.; Bensouici, F.; Belkacemi, H. Efficient photodegradation of azucryl red by copper-doped TiO₂ nanoparticles—Experimental and modeling studies. *Environ. Sci. Pollut. Res.* **2021**, *28*, 57543–57556. [[CrossRef](#)] [[PubMed](#)]
25. Toghan, A.; Abd El-Lateef, H.M.; Taha, K.K.; Modwi, A. Mesoporous TiO₂@g-C₃N₄ composite: Construction, characterization, and boosting indigo carmine dye destruction. *Diam. Relat. Mater.* **2021**, *118*, 108491. [[CrossRef](#)]
26. Idriss, H. Decolorization of malachite green in aqueous solution via MgO nanopowder. *J. Optoelectron. Biomed. Mater. Vol.* **2021**, *13*, 183–192.

27. Idriss, H.; Alakhras, A.; El Khair, H. Malachite green removal from aqueous solutions by MgO (86%). Se (7%). Te (7%) nanocomposites. *Chalcogenide Lett.* **2021**, *18*, 629–638.
28. Modwi, A.; Aissa, B.; Taha, K.K.; Khezami, L.; El Ghoul, J.; Al-Ayed, A.S.; Bououdina, M. Fabrication of (Y₂O₃) n–ZnO nanocomposites by high-energy milling as potential photocatalysts. *J. Mater. Sci. Mater. Electron.* **2021**, *32*, 3415–3430. [[CrossRef](#)]
29. Ahmed, A.S.; Ahamad, T.; Ahmad, N.; Khan, M.Z. Removal enhancement of acid navy blue dye by GO-TiO₂ nanocomposites synthesized using sonication method. *Mater. Chem. Phys.* **2019**, *238*, 121906. [[CrossRef](#)]
30. Zhang, J.-J.; Qi, P.; Li, J.; Zheng, X.-C.; Liu, P.; Guan, X.-X.; Zheng, G.-P. Three-dimensional Fe₂O₃–TiO₂–graphene aerogel nanocomposites with enhanced adsorption and visible light-driven photocatalytic performance in the removal of RhB dyes. *J. Ind. Eng. Chem.* **2018**, *61*, 407–415. [[CrossRef](#)]
31. Harja, M.; Lupu, N.; Chiriac, H.; Herea, D.-D.; Buema, G. Studies on the Removal of Congo Red Dye by an Adsorbent Based on Fly-Ash@ Fe₃O₄ Mixture. *Magnetochemistry* **2022**, *8*, 125. [[CrossRef](#)]
32. Le, T.T.T.; Tran, T.D. Photocatalytic degradation of rhodamine B by C and N codoped TiO₂ nanoparticles under visible-light irradiation. *J. Chem.* **2020**. [[CrossRef](#)]
33. Sriram, G.; Bendre, A.; Altalhi, T.; Jung, H.-Y.; Hegde, G.; Kurkuri, M. Surface engineering of silica based materials with Ni–Fe layered double hydroxide for the efficient removal of methyl orange: Isotherms, kinetics, mechanism and high selectivity studies. *Chemosphere* **2022**, *287*, 131976. [[CrossRef](#)] [[PubMed](#)]
34. Modwi, A.; Al-Ayed, A.S.; Mustafa, D.E.; Bagabas, A.A.; Elamin, M.; Algethami, F.K.; Arasheed, R.; Alfaifi, M.Q.; Alqarni, A.; Alotaibi, F. Ultrasound-assisted green biosynthesis of ZnO nanoparticles and their photocatalytic application. *Z. Für Nat. A* **2021**, *76*, 535–547. [[CrossRef](#)]
35. Yang, F.; Song, Y.; Hui, A.; Wang, Q.; Wang, A. Facile biosynthesis of ZnO/attapulgite nanocomposite for enhanced antimicrobial performance. *Mater. Lett.* **2022**, *323*, 132549. [[CrossRef](#)]
36. Jimoh, A.; Akpeji, B.; Azeez, S.; Ayipo, Y.; Abdulsalam, Z.; Adebayo, Z.; Ajao, A.; Zakariyah, A.; Elemike, E. Biosynthesis of Ag and TiO₂ nanoparticles and the evaluation of their antibacterial activities. *Inorg. Chem. Commun.* **2022**, *141*, 109503. [[CrossRef](#)]
37. Wafi, M.A.E.; Ahmed, M.; Abdel-Samad, H.S.; Medien, H. Exceptional removal of methylene blue and p-aminophenol dye over novel TiO₂/RGO nanocomposites by tandem adsorption-photocatalytic processes. *Mater. Sci. Energy Technol.* **2022**, *5*, 217–231. [[CrossRef](#)]
38. Alsalmeh, A.; Galal, A.; El-Sherbeny, E.F.; Soltan, A.; Abdel-Messih, M.; Ahmed, M. Fabrication of S-scheme TiO₂/g-C₃N₄ nanocomposites for generation of hydrogen gas and removal of fluorescein dye. *Diam. Relat. Mater.* **2022**, *122*, 108819. [[CrossRef](#)]
39. Al-Mamun, M.R.; Karim, M.N.; Nitun, N.A.; Kader, S.; Islam, M.S.; Khan, M.Z.H. Photocatalytic performance assessment of GO and Ag co-synthesized TiO₂ nanocomposite for the removal of methyl orange dye under solar irradiation. *Environ. Technol. Innov.* **2021**, *22*, 101537. [[CrossRef](#)]
40. Zhang, W.; Lan, Y.; Ma, M.; Chai, S.; Zuo, Q.; Kim, K.-H.; Gao, Y. A novel chitosan–vanadium–titanium–magnetite composite as a superior adsorbent for organic dyes in wastewater. *Environ. Int.* **2020**, *142*, 105798. [[CrossRef](#)]
41. Liang, X.; Zhong, Y.; Zhu, S.; Zhu, J.; Yuan, P.; He, H.; Zhang, J. The decolorization of Acid Orange II in non-homogeneous Fenton reaction catalyzed by natural vanadium–titanium magnetite. *J. Hazard. Mater.* **2010**, *181*, 112–120. [[CrossRef](#)]
42. Sanchez Mendez, M.; Lemarchand, A.; Traore, M.; Perruchot, C.; Sassoye, C.; Selmane, M.; Nikravech, M.; Ben Amar, M.; Kanaev, A. Photocatalytic Activity of Nanocoatings Based on Mixed Oxide V-TiO₂ Nanoparticles with Controlled Composition and Size. *Catalysts* **2021**, *11*, 1457. [[CrossRef](#)]
43. Almufarrij, R.S.; Abdulkhair, B.Y.; Salih, M.; Alhamdan, N.M.J.N. Sweep-Out of Tigecycline, Chlortetracycline, Oxytetracycline, and Doxycycline from Water by Carbon Nanoparticles Derived from Tissue Waste. *Nanomaterials* **2022**, *12*, 3617. [[CrossRef](#)] [[PubMed](#)]
44. Elamin, M.R.; Ibaouf, K.H.; Elamin, N.Y.; Adam, F.A.; Alolayan, A.H.; Abdulkhair, B.Y.J.I. Spontaneous Adsorption and Efficient Photodegradation of Indigo Carmine under Visible Light by Bismuth Oxyiodide Nanoparticles Fabricated Entirely at Room Temperature. *Inorganics* **2022**, *10*, 65. [[CrossRef](#)]
45. Navyashree, G.; Hareesh, K.; Sunitha, D.; Nagabhushana, H.; Nagaraju, G. Photocatalytic degradation performance of Nd³⁺-doped V₂O₅ nanostructures. *Mater. Res. Express* **2018**, *5*, 095007. [[CrossRef](#)]
46. Modwi, A.; Abbo, M.; Hassan, E.; Houas, A. Effect of annealing on physicochemical and photocatalytic activity of Cu 5% loading on ZnO synthesized by sol–gel method. *J. Mater. Sci. Mater. Electron.* **2016**, *27*, 12974–12984.
47. Yao, T.; Wang, H. Metal-organic framework derived vanadium-doped TiO₂@ carbon nanotablets for high-performance sodium storage. *J. Colloid Interface Sci.* **2021**, *604*, 188–197. [[CrossRef](#)] [[PubMed](#)]
48. Liu, T.; Yao, T.; Li, L.; Zhu, L.; Wang, J.; Li, F.; Wang, H. Embedding amorphous lithium vanadate into carbon nanofibers by electrospinning as a high-performance anode material for lithium-ion batteries. *J. Colloid Interface Sci.* **2020**, *580*, 21–29. [[CrossRef](#)]
49. Yin, J.; Yang, H.; Kong, W.; Man, J.; Zhou, Z.; Feng, W.; Sun, J.; Wen, Z. Highly compacted TiO₂/C microspheres via in-situ surface-confined intergrowth with ultra-long life for reversible Na-ion storage. *J. Colloid Interface Sci.* **2021**, *582*, 526–534. [[CrossRef](#)]
50. Cha, W.; Chin, S.; Park, E.; Yun, S.-T.; Jurng, J. Photocatalytic performance of V₂O₅/TiO₂ materials prepared by chemical vapor condensation and impregnation method under visible-light. *Powder Technol.* **2014**, *258*, 352–357. [[CrossRef](#)]
51. Chen, C.; Ma, W.; Zhao, J. Semiconductor-mediated photodegradation of pollutants under visible-light irradiation. *Chem. Soc. Rev.* **2010**, *39*, 4206–4219. [[CrossRef](#)]

52. Putluru, S.S.R.; Schill, L.; Godiksen, A.; Poreddy, R.; Mossin, S.; Jensen, A.D.; Fehrmann, R. Promoted V₂O₅/TiO₂ catalysts for selective catalytic reduction of NO with NH₃ at low temperatures. *Appl. Catal. B Environ.* **2016**, *183*, 282–290. [[CrossRef](#)]
53. Li, L.-X.; Xu, D.; Li, X.-Q.; Liu, W.-C.; Jia, Y. Excellent fluoride removal properties of porous hollow MgO microspheres. *New J. Chem.* **2014**, *38*, 5445–5452. [[CrossRef](#)]
54. Kruk, M.; Jaroniec, M. Gas adsorption characterization of ordered organic–inorganic nanocomposite materials. *Chem. Mater.* **2001**, *13*, 3169–3183. [[CrossRef](#)]
55. Yang, W.; Lu, Y.; Zheng, F.; Xue, X.; Li, N.; Liu, D. Adsorption behavior and mechanisms of norfloxacin onto porous resins and carbon nanotube. *Hemical Eng. J.* **2012**, *179*, 112–118. [[CrossRef](#)]
56. Lin, P.; Zhang, Y.; Zhang, X.; Chen, C.; Xie, Y.; Suffet, I.H. The influence of chlorinated aromatics' structure on their adsorption characteristics on activated carbon to tackle chemical spills in drinking water source. *Front. Environ. Sci. Eng.* **2015**, *9*, 138–146. [[CrossRef](#)]
57. Naghizadeh, A.; Karimi, A.; Derakhshani, E.; Esform, A. Single-walled carbon nanotubes (SWCNTs) as an efficient adsorbent for removal of reactive dyes from water solution: Equilibrium, kinetic, and thermodynamic. *Environ. Qual. Manag.* **2022**, *31*, 133–140. [[CrossRef](#)]
58. Sallal, H.A.; Abdul-Hameed, A.A.; Othman, F. Preparation of Al₂O₃/MgO Nano-Composite Particles for Bio-Applications. *Eng. Technol. J.* **2020**, *38*, 586–593. [[CrossRef](#)]
59. Elamin, M.R.; Abdulkhair, B.Y.; Elzupir, A.O. Removal of ciprofloxacin and indigo carmine from water by carbon nanotubes fabricated from a low-cost precursor: Solution parameters and recyclability. *Ain Shams Eng. J.* **2023**, *14*, 101844. [[CrossRef](#)]
60. Acharya, J.; Sahu, J.; Mohanty, C.; Meikap, B.C. Removal of lead (II) from wastewater by activated carbon developed from Tamarind wood by zinc chloride activation. *Chem. Eng. J.* **2009**, *149*, 249–262. [[CrossRef](#)]
61. Salam, M.A.; Al-Zhrani, G.; Kosa, S.A. Chemistry, E. Removal of heavy metal ions from aqueous solution by multi-walled carbon nanotubes modified with 8-hydroxyquinoline: Kinetic study. *J. Ind. Eng. Chem.* **2014**, *20*, 572–580. [[CrossRef](#)]
62. Largitte, L.; Pasquier, R. A review of the kinetics adsorption models and their application to the adsorption of lead by an activated carbon. *Chem. Eng. Res. Des.* **2016**, *109*, 495–504. [[CrossRef](#)]
63. Wierzbicka, E.; Kusmieriek, K.; Swi, A.; Legocka, I. Efficient rhodamine b dye removal from water by acid-and organo-modified halloysites. *Minerals* **2022**, *12*, 350. [[CrossRef](#)]
64. Yen Doan, T.H.; Minh Chu, T.P.; Dinh, T.D.; Nguyen, T.H.; Tu Vo, T.C.; Nguyen, N.M.; Nguyen, B.H.; Pham, T.D. Adsorptive removal of rhodamine B using novel adsorbent-based surfactant-modified alpha alumina nanoparticles. *J. Anal. Methods Chem.* **2020**. [[CrossRef](#)] [[PubMed](#)]
65. Belachew, N.; Tadesse, A.; Kahsay, M.H.; Meshesha, D.S.; Basavaiah, K. Synthesis of amino acid functionalized Fe₃O₄ nanoparticles for adsorptive removal of Rhodamine B. *Appl. Water Sci.* **2021**, *11*, 1–9. [[CrossRef](#)]
66. Liu, Y.; Liu, Y.-J. Biosorption isotherms, kinetics and thermodynamics. *Sep. Purif. Technol.* **2008**, *61*, 229–242. [[CrossRef](#)]
67. Oyetade, O.A.; Nyamori, V.O.; Martincigh, B.S.; Jonnalagadda, S.B. Effectiveness of carbon nanotube–cobalt ferrite nanocomposites for the adsorption of rhodamine B from aqueous solutions. *RSC Adv.* **2015**, *5*, 22724–22739. [[CrossRef](#)]
68. Ojemaye, M.O.; Okoh, A.I. Multiple nitrogen functionalized magnetic nanoparticles as an efficient adsorbent: Synthesis, kinetics, isotherm and thermodynamic studies for the removal of rhodamine B from aqueous solution. *Sci. Rep.* **2019**, *9*, 1–13. [[CrossRef](#)]
69. Peng, L.; Qin, P.; Lei, M.; Zeng, Q.; Song, H.; Yang, J.; Shao, J.; Liao, B.; Gu, J. Modifying Fe₃O₄ nanoparticles with humic acid for removal of Rhodamine B in water. *J. Hazard. Mater.* **2012**, *209*, 193–198. [[CrossRef](#)]
70. Konicki, W.; Siber, D.; Narkiewicz, U. Removal of Rhodamine B from aqueous solution by ZnFe₂O₄ nanocomposite with magnetic separation performance. *Pol. J. Chem. Technol.* **2017**, *19*, 65–74. [[CrossRef](#)]
71. Motahari, F.; Mozdianfard, M.R.; Salavati-Niasari, M.J.P.S.; Protection, E. Synthesis and adsorption studies of NiO nanoparticles in the presence of H₂acacen ligand, for removing Rhodamine B in wastewater treatment. *Process Saf. Environ. Prot.* **2015**, *93*, 282–292. [[CrossRef](#)]
72. Nazir, M.A.; Najam, T.; Jabeen, S.; Wattoo, M.A.; Bashir, M.S.; Shah, S.S.A.; ur Rehman, A. Facile synthesis of Tri-metallic layered double hydroxides (NiZnAl-LDHs): Adsorption of Rhodamine-B and methyl orange from water. *Inorg. Chem. Commun.* **2022**, *145*, 110008. [[CrossRef](#)]
73. Letshwenyo, M.W.; Mokgosi, S. Investigation of water treatment sludge from drinking water treated with Zetafloc 553I coagulant for phosphorus removal from wastewater. *J. Environ. Manag.* **2021**, *282*, 111909. [[CrossRef](#)] [[PubMed](#)]
74. Demirbas, O.; Calimli, M.H.; Kuyuldar, E.; Alma, M.H.; Nas, M.S.; Sen, F.J.B. Equilibrium, kinetics, and thermodynamic of adsorption of enzymes on diatomite clay materials. *BioNanoScience* **2019**, *9*, 474–482. [[CrossRef](#)]
75. Aarab, N.; Hsini, A.; Esseki, A.; Laabd, M.; Lakhmiri, R.; Albourine, A. Removal of an emerging pharmaceutical pollutant (metronidazole) using PPy-PANi copolymer: Kinetics, equilibrium and DFT identification of adsorption mechanism. *Groundw. Sustain. Dev.* **2020**, *11*, 100416. [[CrossRef](#)]

76. Vasudevan, S.; Lakshmi, J.J.W.S. Studies relating to an electrochemically assisted coagulation for the removal of chromium from water using zinc anode. *Water Sci. Technol. Water Supply* **2011**, *11*, 142–150. [[CrossRef](#)]
77. Inglezakis, V.J.; Zorpas, A.A. Heat of adsorption, adsorption energy and activation energy in adsorption and ion exchange systems. *Desalination Water Treat.* **2012**, *39*, 149–157. [[CrossRef](#)]

Disclaimer/Publisher’s Note: The statements, opinions and data contained in all publications are solely those of the individual author(s) and contributor(s) and not of MDPI and/or the editor(s). MDPI and/or the editor(s) disclaim responsibility for any injury to people or property resulting from any ideas, methods, instructions or products referred to in the content.